ADVANCED MATERIALS
www.advmat.de

Design of Aligned Porous Carbon Films with Single-Atom Co–N–C Sites for High-Current-Density Hydrogen Generation

Rui Liu, Zhichao Gong, Jianbin Liu, Juncai Dong, Jiangwen Liao, Huan Liu, Haikang Huang, Jingjing Liu, Minmin Yan, Kang Huang, Haisheng Gong, Jian Zhu, Chunyu Cui, Gonglan Ye,* and Huilong Fei**

Metal- and nitrogen-doped carbon (M–N–C) materials as a unique class of single-atom catalysts (SACs) have increasingly attracted attention as the replacement of platinum for the hydrogen evolution reaction (HER); however, their employment as HER electrodes at high current densities of industrial level remains a grand challenge. Herein, an aligned porous carbon film embedded with single-atom Co–N–C sites of exceptional activity and stability at high current densities is designed. Within the film, the atomic CoN_x moieties exhibit high intrinsic activity, while the multiscale porosity of the carbon frameworks with vertically aligned microchannels afford facilitated mass transfer under the conditions of high production rate and ultrathick electrodes. Moreover, the superwetting properties of the film promote electrolyte wetting and ensure the timely removal of the evolving H_2 gas bubbles. The as-designed film can work as an efficient HER electrode to deliver 500 and 1000 mA cm^{-2} in acid at overpotentials of 272 and 343 mV, respectively, and can operate uninterruptedly and stably at 1000 mA cm^{-2} for at least 32 h under static conditions. These findings pave the road toward the rational design of SACs with improved activity and stability at high current densities in gas-evolving electrocatalytic processes.

1. Introduction

Hydrogen (H_2) is a clean and renewable energy carrier, making it an attractive alternative to the diminishing fossil fuel. The key prerequisite to enable the hydrogen-based energy system is the development of efficient and cost-effective methods for H_2 production.[1] Among the various approaches available, electrochemical reduction of water through the hydrogen evolution reaction (HER) is desirable with advantages like cleanness, sustainability, and high purity of product.[2,3] The efficiency of HER relies on the use of high-performance electrocatalysts to enhance its kinetics. While Pt catalysts are most active toward HER, their high cost and low abundancy impede the large-scale implantation. Consequently, it is imperative to develop alternative catalysts based on earth-abundant and inexpensive elements.[4–6] On the other hand, for practical industrial applications, the current densities could be higher than 500 or even 1000 mA cm^{-2} for high-rate H_2 production.[7–9] The operation of catalysts under such high current densities is challenging as it requires not only the high intrinsic activity of catalysts, but also abundant active sites, fast mass transport for both liquid electrolyte and vigorously evolved gas bubbles, as well as good thermal, electrochemical and mechanical stabilities.[10]

Single-atom catalysts (SACs), with isolated metal active sites dispersed on certain supports, have received extensive attention owing to their combined merits of homogeneous and heterogeneous catalysts.[11–14] Metal–nitrogen–carbon (M–N–C) materials

R. Liu, Z. Gong, J. Liu, H. Huang, J. Liu, M. Yan, K. Huang, H. Gong, J. Zhu, C. Cui, G. Ye, H. Fei
Advanced Catalytic Engineering Research Center of the Ministry of Education
State Key Laboratory for Chemo/Biosensing and Chemometrics and College of Chemistry and Chemical Engineering
Hunan University
Changsha 410082, China
E-mail: glye@hnu.edu.cn; hlfei@hnu.edu.cn

The ORCID identification number(s) for the author(s) of this article can be found under https://doi.org/10.1002/adma.202103533.

DOI: 10.1002/adma.202103533

J. Dong, J. Liao
Beijing Synchrotron Radiation Facility
Institute of High Energy Physics
Chinese Academy of Sciences
Beijing 100049, P. R. China
E-mail: dongjc@ihep.ac.cn

H. Liu
Key Laboratory of Bio-Inspired Smart Interfacial Science and Technology of Ministry of Education
School of Chemistry
Beijing Advanced Innovation Center for Biomedical Engineering and International Research Institute for Multidisciplinary Science
Beihang University
Beijing 100191, P. R. China

with MN_x moieties supported on carbon substrate represent a unique class of SACs for their good electrical conductivity, high (electro-)chemical stability and large surface area, making them highly suitable for electrocatalytic applications.[15–18] Particularly, M–N–C materials are considered to be promising HER catalysts and considerable progress has been achieved, with efforts focused on the exploration of new synthetic strategies, the optimization in intrinsic activity manifested as onset overpotential (η) and turnover frequency (TOF), and the fundamental understanding of the active site structure and reaction mechanism.[19–22]

However, few attempts have been made to develop M–N–C HER catalysts capable of delivering industrially relevant current densities. It is noted that the previously reported HER catalysts based on M–N–C materials (and other types of SACs as well) were mostly evaluated at low current densities (typically < 100 mA cm^{-2}, Figure S1, Supporting Information).[23,24] The challenges of operating M–N–C catalysts at high current densities are multifold. First, there are insufficient number of active sites in M–N–C materials as a result of the limited metal loading and low utilization of the MN_x active sites. This can be ascribed to the pyrolysis treatment typically used during the preparation of M–N–C catalysts as the metal contents had to be kept low so as to prevent the high-temperature aggregation of metal atoms and to the fact that there are large portions of inaccessible active sites that are buried within the carbon matrix.[25,26] To partially overcome this limit, strategies have been developed to improve the utilization of active sites and mass transport by modifying the pyrolysis process (e.g., template-assisted pyrolysis, space-confined pyrolysis) that can result in enhanced porosity and surface area.[27,28] Alternatively, one could increase the loading of catalysts on the current collector and thus the electrode thickness, resulting in the increase of the active site density on the geometrical area basis. Unfortunately, the majorities of existing M–N–C materials were synthesized in powdery form and the catalyst loading in the slurry-coated electrode was usually smaller than 1 mg cm^{-2} as overthick electrode could suffer from insufficient transport of charges (electrons and ions) as well as the fracture and delamination issues.[29,30] Second, at high current densities, mass transfer of the reactants in the electrolyte and gaseous products becomes increasingly rate limiting.[31] Especially, the H_2 bubbles could severely block the solid–liquid interfaces, causing unfavorable mass transport, ohmic resistance, and kinetic loss.[32] Another concern associated with H_2 bubbles is the peeling off of catalysts due to the concentrated local stress imposed by the detachment of bubbles, leading to degraded activity and stability.[33] While gas management has recently been investigated to improve the performance of nanoparticulate catalysts under realistic conditions by for example constructing superwetting electrodes,[32,34,35] it remains largely unexplored in single-atom M–N–C counterparts. Above all, the key to render M–N–C catalysts with high-rate capability is the systematic optimization of the intrinsic activity, number of active sites, and mass transfer efficiency.

Here, we present a strategy to enable a highly active and stable high-current-density HER electrode based on M–N–C (M=Co) materials by incorporating the single-atom Co–N–C sites into an aligned porous carbon film (denoted as Co–NC–AF thereafter). The design principle is illustrated in **Figure 1**. The Co–N–C sites possess high intrinsic activity of near-zero onset η and small charge transfer resistance to facilitate the HER kinetics. The free-standing carbon film with vertically aligned macropores through the electrode and nanopores within the networks of carbon walls contribute to the unimpeded ion and gas transport. The multiscale porosity and free-standing features are also beneficial for enriching the active sites by providing highly exposed solid–liquid–gas interfaces and permitting high catalysts loading up to 6 mg cm^{-2} without compromising the mass transfer efficiency, in strong contrast to conventional drop-cast electrodes. Moreover, the nanocarbon-array electrode with rough surface texture has desirable surface wettability of superhydrophilicity and under-water superaerophobicity that can facilitate the access of electrolyte and the release of small-size H_2 bubbles. With the combined benefits, Co–NC–AF as an HER electrode is able to deliver high current densities up to 500 and 1000 mA cm^{-2} in 0.5 M H_2SO_4 at η of 272 and 343 mV, respectively, and run continuously and steadily at 1000 mA cm^{-2} for at least 32 h under static condition (i.e., without forced convection).

2. Results and Discussion

2.1. Synthesis and Structural Characterization

A schematic illustrating the preparation process of Co–NC–AF is shown in Figure S2 (Supporting Information). Briefly, ethanol-mediated aqueous suspension containing strongly oxidized multiwall carbon nanotubes (O-MWCNTs) and controlled amounts of cobalt salts was first hydrothermally self-assembled into a hydrogel, which can be thinned into a film with different thicknesses. The addition of ethanol as cosolvent is critical as it works as the antifreeze to decrease the freezing point, which can affect the crystallization behavior of ice growth in the followed freezing treatment. The film was then subjected to an ice-templated unidirectional freezing treatment, during which freezing-induced phase separation drives the O-MWCNTs to accumulate along the growing direction of ice crystals. The entrapped O-MWCNTs can form an aligned porous carbon framework after the sublimation of the ice by freeze-drying. After that, the film was thermally annealed under Ar/NH_3 atmosphere to eventually obtain Co–NC–AF. NH_3 was introduced as N source to coordinate with the Co atoms to form CoN_x moieties as well as to incorporate N dopants into the graphene lattices. Optical images in **Figure 2**a show the monolithic structure of a 3D and film-shaped Co–NC–AF. The top view of scanning electron microscopy (SEM) reveals that Co–NC–AF has a high surface roughness with uniformly distributed pores in the size range of 10–20 μm (Figure 2b). Cross-sectional SEM images denote that the carbon film has long-range vertical alignments and the channel width is ≈20 μm (Figure 2c,d; and Figure S3, Supporting Information). Carbon structures bridging between parallel carbon layers were observed, which could enhance the structural integrity of the film for improved mechanical strength and electrical conductance. Enlarged SEM image in Figure 2e shows that the lamellar wall consists of highly overlapped and entangled fibrous nanocarbons, which are revealed by transmission electron microscopy (TEM)

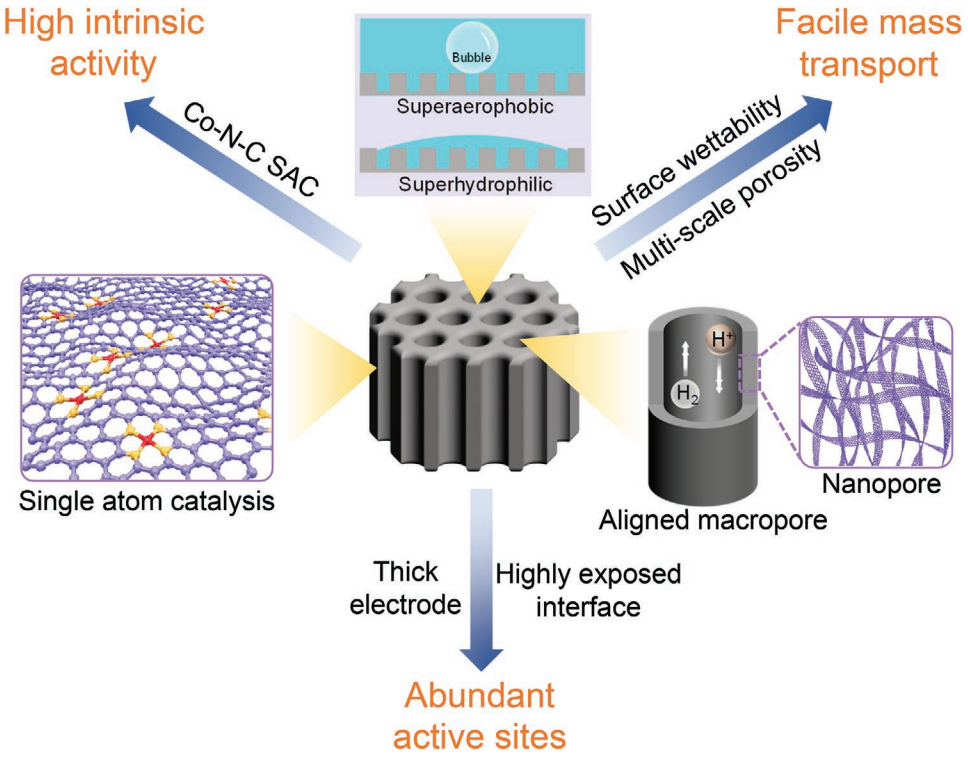

Figure 1. Design strategy of Co–NC–AF electrode toward high-current-density hydrogen production. The atomically dispersed Co–N–C sites with high intrinsic activity can significantly enhance the kinetics of HER process. The aligned macropores and nanopores among the carbon networks enable the efficient utilization of the two-phase contact area between catalyst and electrolyte for the ultrathick electrode, creating abundant active sites. The multiscale porosity and superwetting properties (superhydrophilicity and superaerophobicity) of the electrode can effectively improve the mass transport efficiency by facilitating the permeation of liquid electrolyte and the removal of gas products.

images to be MWCNTs and graphene sheets derived from the oxidative partial unzipping of MWCNTs (Figure 2f; and Figure S4, Supporting Information). Within this architecture, the intact MWCNTs serve as the structural skeleton to improve the rigidity and electrical conductivity of the carbon networks, while the graphene sheets act as the substrates for dispersing single-atom CoN_x sites. The nitrogen adsorption–desorption isotherms reveal that Co–NC–AF has a Brunauer–Emmett–Teller (BET) specific surface area of 145.0 $m^2\ g^{-1}$ and the pore size distributions suggest the formation of mesopores with the pore size centered at ≈3.7 nm (Figure 2g; and Figure S5, Supporting Information). Raman spectrum and X-ray diffraction (XRD) pattern detect the defective feature of the graphitized carbon (Figures S6 and S7, Supporting Information).

The electrode tortuosity, defined as the ratio of the actual path length to the straight-through path length of the electrode, is critical in obtaining effective mass transfer, especially for thick electrodes and high-rate applications.[29,36] The tortuosity of Co–NC–AF was measured by the alternating current (AC) impedance method (Figure 2h; and Figure S8, Supporting Information).[36] For comparison, a control sample (denoted as Co–NC–RF) with Co–N–C sites dispersed in a randomly oriented porous film was prepared and its morphology and porous structure was characterized by SEM and BET surface area measurement (Figures S9 and S10, Supporting Information). Benefiting from the aligned microchannels of Co–NC–AF, its tortuosity value of ≈1.7 is considerably lower than that of Co–NC–RF (≈2.1). It is noted that these values are much lower than those typically found in slurry-based electrodes (3–30).[37] The aligned carbon arrays in Co–NC–AF also provide a conductive highway to transport electrons, as suggested by its much higher electrical conductivity (22.4 S m^{-1}) than that of Co–NC–RF (2.1 S m^{-1}) (Figure 2i; and Figure S11, Supporting Information). The electrochemically active surface area (ECSA) was estimated by measuring the double-layer capacitance (C_{dl}) (Figure 2j; and Figure S12, Supporting Information). The C_{dl} of Co–NC–AF is 336 mF cm^{-2}, which is significantly higher than that of Co–NC–RF (128 mF cm^{-2}), manifesting the role of aligned macropores in the exposure of electroactive interfaces.

2.2. Analysis of Composition and Atomic Structure

The composition of Co–NC–AF and control samples was probed by X-ray photoelectron spectroscopy (XPS) (**Figure 3**a; and Figure S13, Supporting Information), which shows the presence of C, N, and O peaks. The XPS signal from Co element is insignificant due to its low content, which can be determined by inductively coupled plasma mass spectrometry (ICP-MS). As summarized in the inset of Figure 3a, Co–NC–AF consists of 0.5 wt% Co, 4.5 wt% N, 5.2 wt% O, and 89.8 wt% C. The XPS detailed scan of Co presents two major peaks at the binding energy of 780.4 and 795.9 eV (Figure 3b; and Figure S14, Supporting Information), corresponding to the $2p_{3/2}$ and $2p_{1/2}$

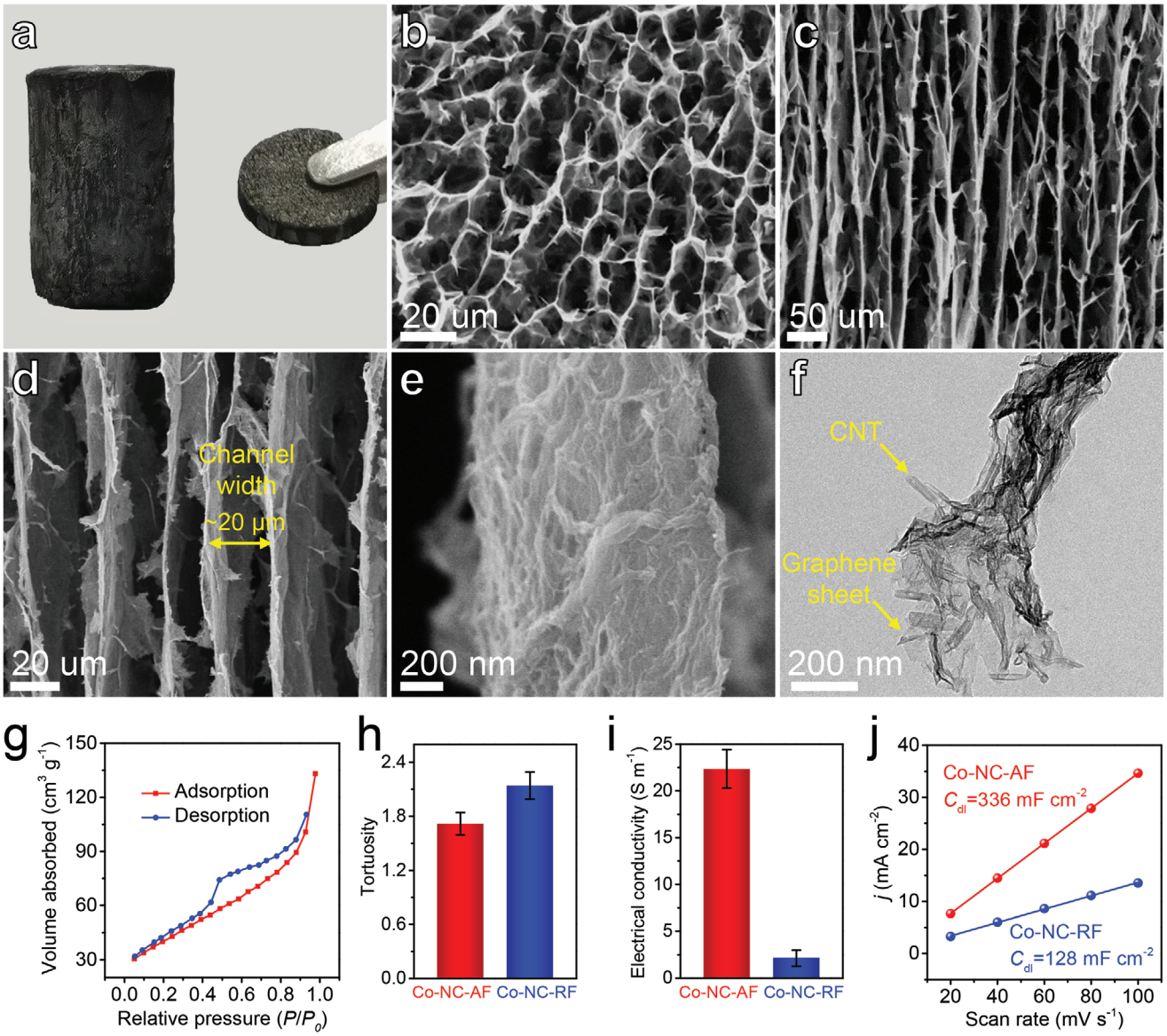

Figure 2. Characterization of the morphology and porous structure. a) Optical image of a monolithic and film-shaped Co–NC–AF. b) Top-view SEM image of Co–NC–AF. The surface has high roughness and high porosity. c) Cross-sectional SEM image of Co–NC–AF, showing the aligned microchannels. d) Enlarged view of the view in (c). The channel width is ≈20 µm. e) SEM image showing the wall structure composed of entangled fibrous carbons. f) TEM image of the interconnected MWCNTs and graphene sheets. g) Nitrogen adsorption and desorption curves of Co–NC–AF. h–i) Comparison of the tortuosity (h) and electrical conductivity (i) of Co–NC–AF and Co–NC–RF. j) Electrochemical double layer capacitance (C_{dl}) of Co–NC–AF and Co–NC–RF.

levels, respectively, suggesting the Co is in ionic state.[38] The C 1s, N 1s, and O 1s XPS were provided in Figures S15 and S16 (Supporting Information). Energy-dispersive X-ray spectroscopy (EDS) mapping suggests the homogeneous spatial distribution of Co, C, N, and O elements on the carbon matrix (Figure S17, Supporting Information). Observation by annular dark-field scanning transmission electron microscopy (ADF-STEM) reveals a uniform dispersion of some individual bright dots with size of ≈2 Å, corresponding to isolated single Co atoms (Figure 3c).

The chemical state and local structure of the Co atoms in Co–NC–AF were studied by Co K-edge X-ray absorption fine structure (XAFS) spectroscopy. As shown in Figure 3d, the X-ray absorption near-edge structure (XANES) profile for Co–NC–AF is obviously distinct from those of the bulk Co and CoO references. The comparison of the Co K-edge position (energy corresponding to half the edge step height) indicates that the valence state of Co atoms in Co–NC–AF is about +2. Moreover, the pre-edge 1s-to-3d transition peak demonstrates stronger intensity in Co–NC–AF than that of CoO, suggesting a broken D_{4h} symmetry around the Co atoms with a rather distorted or defective graphene architecture.[39] Figure 3e shows the Fourier transform (FT) of extended X-ray absorption fine structure (EXAFS) for Co–NC–AF and reference samples. Co–NC–AF

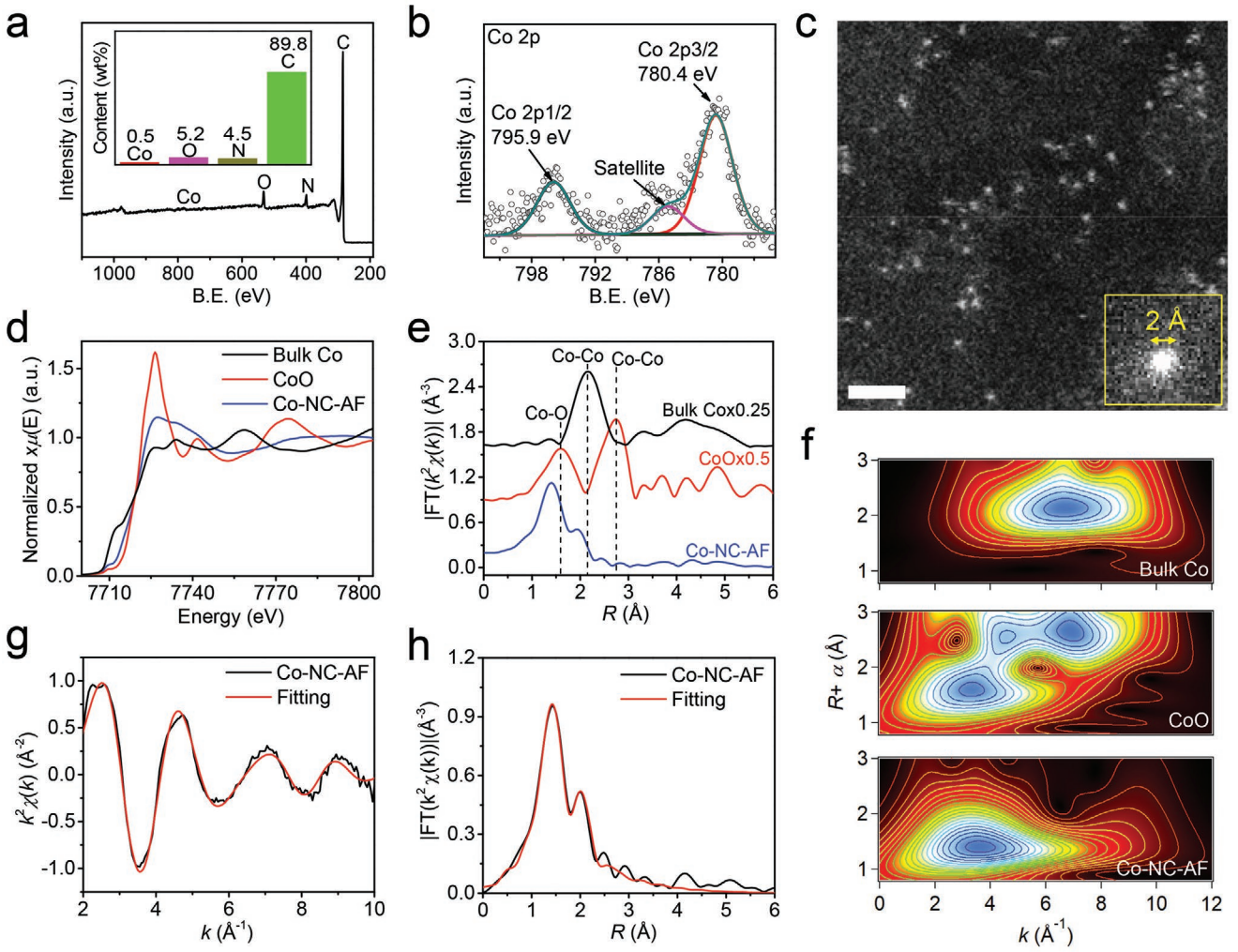

Figure 3. Analysis of composition and atomic structure. a) XPS survey spectra of Co–NC–AF. The inset chart shows the weight percentages of cobalt, nitrogen, oxygen, and carbon measured by XPS and ICP–MS. b) High-resolution XPS Co 2p spectrum. c) ADF–STEM image of Co–NC–AF, showing the evenly dispersed Co atoms in the carbon matrix. The inset shows an individual cobalt atom with size of ≈2 Å. Scale bar: 1 nm. d) The K-edge XANES spectra of Co–NC–AF and reference samples (bulk cobalt and cobalt oxide). e) Fourier transformed magnitudes of the K-edge EXAFS signals of Co–NC–AF and reference samples. f) Wavelet transforms for the k^2-weighted EXAFS of Co–NC–AF and reference samples. g,h) Co K-edge EXAFS analysis of Co–NC–AF in *k* space (g) and *R* space (h), respectively, with the fitted curve (red line) superimposed on the experimental one (black line). The measured and calculated spectra show excellent agreement.

exhibits a major peak at 1.42 Å and a minor peak at 1.94 Å, while the Co–O peak at 1.60 Å for the CoO_6 octahedra in CoO and the Co–Co peak at 2.16 Å in bulk Co were not detected, suggesting the Co atoms in Co–NC–AF are atomically dispersed and stabilized by light elements. This is in agreement with the XRD result that shows no peaks derived from crystalline Co (Figure S6, Supporting Information). Further, EXAFS wavelet transform (WT) analysis was performed for its capability to discriminate the backscattering atoms and provide powerful resolution in both *k* space and *R* space.[40] As shown in Figure 3f, Co–NC–AF exhibits only one intensity maximum at ≈4.0 $Å^{-1}$ that can be assigned to the Co–N/O/C contributions and the intensity maximum indexed to Co–Co scattering at ≈6.0 $Å^{-1}$ was not observed, confirming the atomic dispersion of Co. Quantitative structural results for the CoN_x moiety in Co–NC–AF were extracted by least-squares EXAFS curve-fitting analysis. As seen in Figure 3g,h, the *k* space and *R* space best fitting curves match well with the experimental ones. Based on the fitting parameters (Table S1, Supporting Information), the first shell coordination number of the central Co atom to N(O) atoms was estimated to be 3.5 at the distance of 1.87 Å.

2.3. Surface Wettability

To study the surface wettability of Co–NC–AF, the contact angle (CA) tests and adhesive force of gas bubbles were performed. For comparison, a control sample (denoted as Co–NC–CF) with Co–N–C sites embedded in a compact film was prepared and its fabrication process is described in the Experimental Section. SEM images show that Co–NC–CF is composed of compactly stacked carbon layers and its surface is smooth with low

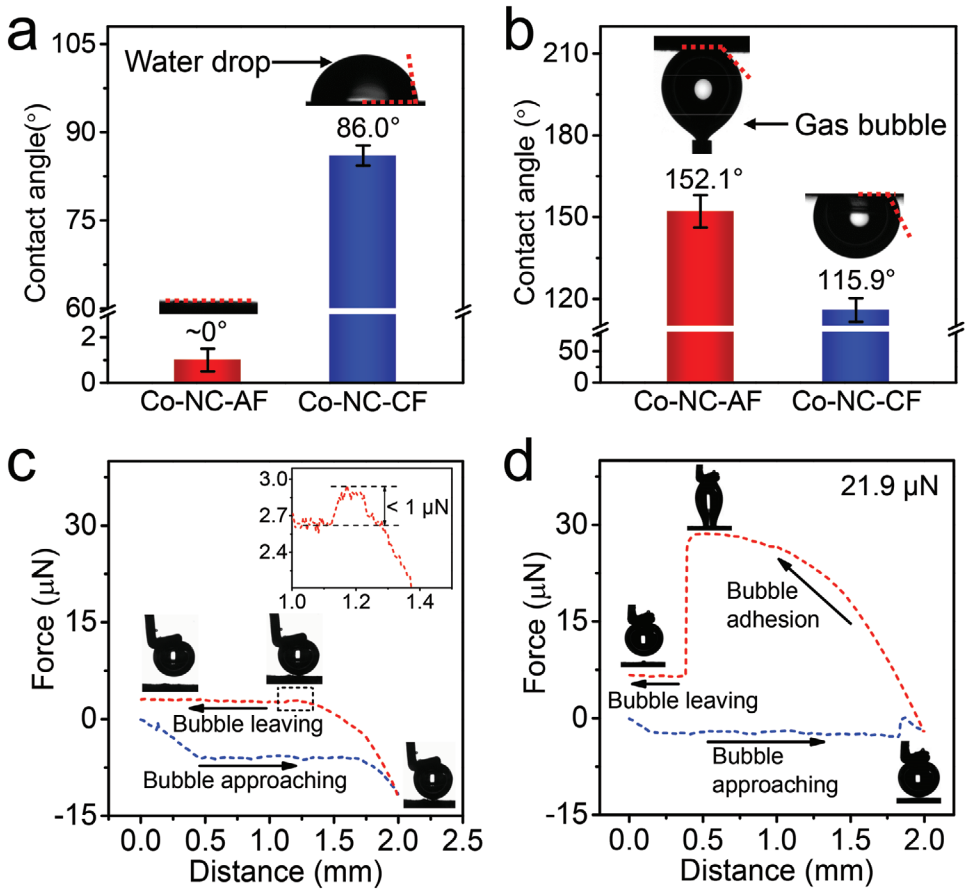

Figure 4. Characterization of surface wettability. a) Contact angles of water droplet on the surface of Co–NC–AF and Co–NC–CF. Co–NC–AF with close-to-zero contact angle is superhydrophilic and Co–NC–CF with contact of ≈86.0° is much less hydrophilic. b) Underwater gas-bubble contact angles of Co–NC–AF and Co–NC–CF. Co–NC–AF with contact angles of ≈152.1° is much more aerophobic than Co–NC–CF (≈115.9°). c,d) Gas bubble adhesive force measurements of Co–NC–AF (c) and Co–NC–CF (d). Co–NC–AF shows negligible bubble adhesive force, while Co–NC–CF exhibits large bubble adhesive force of 21.9 μN. The insets show the bubble states in the corresponding measurement process.

roughness (Figure S18, Supporting Information). For the water CA measurements (**Figure 4**a), Co–NC–AF with CA ≈0° is superhydrophilic and water droplets spread immediately once in contact with the surface. The superhydrophilicity of the surface and the capillary force induced by the microchannels can infiltrate the electrolyte deep into the Co–NC–AF electrode for highly exposed solid–liquid interface.[41] In comparison, Co–NC–CF is much less hydrophilic with CA ≈86.0°. For the underwater gas bubble CA (Figure 4b), Co–NC–AF with CA ≈152.1° is superaerophobic, while Co–NC–CF has a much smaller CA ≈115.9°. Gas bubble adhesive force measurements demonstrate that Co–NC–AF presents a negligible adhesive force (< 1 μN) with little change in bubble shape during the measurement (Figure 4c). The dynamic process of the gas bubble bouncing phenomena on Co–NC–AF was recorded by high-speed camera (Figure S19 and Movie S1, Supporting Information), confirming the extremely low bubble adhesion. By contrast, Co–NC–CF possesses an appreciable adhesive force of 21.9 μN, giving rise to an apparent deformation of the gas bubble when detaching the electrode surface (Figure 4d). The superaerophobicity of Co–NC–AF can be ascribed to its hydrophilicity and porous structure. As reported previously, the porous structure could offer a discontinuous three phase (solid–liquid–gas) contact line (TPCL) that minimizes the gas bubble adhesion on the electrode. At the same time, when the hydrophilic film is immersed into aqueous medium, it could be spontaneously wetted by water that acts as "water cushion" to reduce the adhesion of gas bubble.[42,43] In strong contrast, Co–NC–CF with flat surface and poor hydrophilicity has a continuous TPCL and therefore strong interaction with gas bubbles, which is also the commonly encountered situation in conventional electrodes containing carbon that is hydrophobic in nature. Overall, the superwetting properties of Co–NC–AF could enhance the mass transfer efficiency by facilitating the access of electrolyte and the release of bubbles, which are crucial for gas-evolving electrodes with high-current capability.

2.4. Electrocatalytic Hydrogen Evolution

Co–NC–AF was directly applied as the working electrode with no addition of polymer binder or conductive additive, which not only simplifies the electrode fabrication process but also circumvents the issues of metal dissolution in acid and catalyst layer delamination when metal-based current collectors (e.g., Cu and Ni foams) are used in electrode preparation

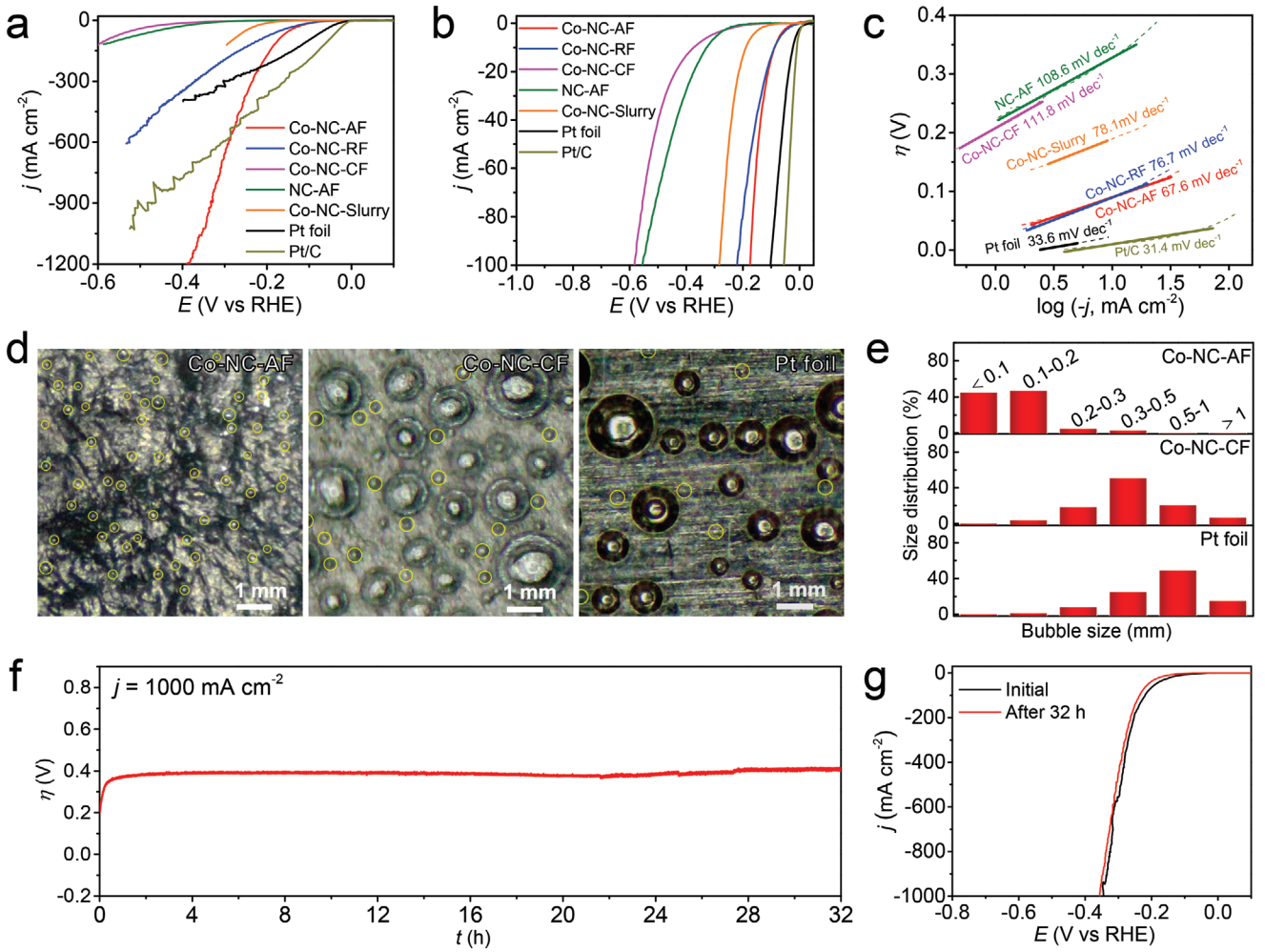

Figure 5. Electrocatalytic performance toward HER. a) HER activity evaluated by linear sweep voltammetry in 0.5 M H_2SO_4 at the scan rate of 5 mV s^{-1} for Co–NC–AF, Co–NC–RF, Co–NC–CF, NC–AF, Co–NC–Slurry along with Pt foil and Pt/C as reference point. b) Expanded view of the low overpotential region in (a). The reaction starts at ≈0 V for Co–NC–AF and the current density increases sharply upon the increase of overpotential. c) Tafel slopes of different catalysts obtained from the polarization curves in (b). d) Snapshots of H_2 bubbles detaching from Co–NC–AF, Co–NC–CF, and Pt foil at the current density of 100 mA cm^{-2}. e) Bubble size distributions on Co–NC–AF, Co–NC–CF, and Pt foil. f) Stability of Co–NC–AF evaluated by the galvanostatic technique at the current density of 1000 mA cm^{-2} for 32 h. The data are presented with 100% *IR*-correction. g) Polarization curves of Co–NC–AF before and after the galvanostatic stability test.

by drop-casting method.[44] Measurements of HER activity were performed in a typical three-electrode configuration in N_2-saturated 0.5 M H_2SO_4 electrolyte. The optimal Co–NC–AF electrode has a thickness of 1.5 mm and areal mass loading of 6.0 mg cm^{-2} (Figures S20 and S21, Supporting Information). It can be seen from the polarization curves in **Figure 5**a that Co–NC–AF is able to sustain exceptionally high current densities, reaching 100, 300, 500, and 1000 mA cm^{-2} at η = 174, 234, 272, and 343 mV, respectively. The faradaic efficiency of H_2 production is determined to be 98.9% by comparing the theoretically calculated amounts of H_2 and those collected via a Hoffman apparatus setup (Figure S22, Supporting Information). The presented activity of Co–NC–AF compares favorably to nanoparticulate catalysts with high-current-density capability (Figure S23 and Table S2, Supporting Information), such as HC-MoS_2/Mo_2C (η_{100} = 329 mV, η_{500} = 382 mV, η_{1000} = 412 mV),[10] $Nb_{1.35}S_2$ (η_{100} = 209 mV, η_{500} = 278 mV, η_{1000} = 370 mV),[31] Nb-WS_2 (η_{100} = 200 mV, η_{500} = 280 mV, η_{1000} = 320 mV),[45] α-MoB_2 (η_{100} = 214 mV, η_{500} = 282 mV, η_{1000} = 334 mV),[46] and MoS_2/Mo_2C (η_{100} = 179 mV, η_{500} = 219 mV, η_{1000} = 227 mV).[41] To examine the origin for the high activity of Co–NC–AF, a series of control samples were tested and compared, including Co–NC–RF, Co–NC–CF, NC–AF (without CoN_x sites) and Co–NC-Slurry prepared by conventional drop-casting method. Pt foil and Pt/C were also included for reference purpose. By comparison, NC–AF exhibits negligible activity, suggesting the critical role of the atomic CoN_x active sites. Co–NC–RF needs larger η of 219, 369, and 483 mV to deliver 100, 300, and 500 mA cm^{-2}, respectively, highlighting the importance of pore alignment. Moreover, Co–NC–CF and Co–NC–Slurry show much lower activity as a result of their poor porosity and thus limited ECSA (Figures S24 and S25, Supporting Information), and are unable to deliver high current densities beyond ≈150 mA cm^{-2} due to the blockage of active sites by the accumulated H_2 bubbles on

the electrode surface. For the flat Pt foil and Pt/C, their activity is higher than that of Co–NC–AF at current densities lower than ≈250 and ≈500 mA cm^{-2}, respectively, but becomes inferior at higher current densities due to the limitation in mass transport efficiency. Interestingly, the performance of Pt/C at high current densities can be enhanced by drop-casting the Pt/C slurry on NC–AF (Figure S26, Supporting Information), suggesting the generality of the aligned porous carbon film in enhancing the mass transport efficiency of different catalytically active species. The expanded view of the low-current-density region reveals that Co–NC–AF has a close-to-zero onset η (23 mV, defined at the current density of 0.3 mA cm^{-2}) and needs 87 mV to deliver the benchmark current density of 10 mA cm^{-2} (Figure 5b); additionally, electrochemical impedance spectroscopy (EIS) determines that it has a small charge transfer resistance (0.28 Ω at η = 30 mV) that is similar to Pt foil (0.36 Ω) (Figure S27, Supporting Information), indicating the high intrinsic activity of Co–NC–AF. It is worth noting that Co–NC–AF and Co–NC–RF have comparable intrinsic activity and present similar profiles of polarization curves at low current densities, suggesting that the dramatic enhancement in the high-current-density activity of Co–NC–AF compared to Co–NC–RF can be ascribed to the improved mass transfer efficiency resulted from the aligned porous structures. This is further confirmed by the ECSA-normalized LSV polarization curves, showing that Co–NC–AF and Co–NC–RF have similar ECSA-normalized activity (Figure S28, Supporting Information). Figure 5c displays the Tafel slopes of the polarization curves that provide insight into the HER pathways on the catalysts. Co–NC–AF presents a small Tafel slope of 67.6 mV dec^{-1}, indicating that the HER process most likely proceeds sequentially through the Volmer step ($H^+ + e^- \rightarrow H_{ads}$) and Heyrovsky step ($H^+ + e^- + H_{ads} \rightarrow H_2$), consistent to previously reported Co–N–C catalysts.[19,47] In comparison, Co–NC–RF, Co–NC–CF, Co–NC–Slurry, and NC–AF exhibit Tafel slope values of 76.7, 111.8, 78.1, and 108.6 mV dec^{-1}, respectively. By extrapolating the Tafel plots to η = 0 mV, the exchange current density (j_0) of Co–NC–AF was calculated to be 0.47 mA cm^{-2} that is much higher than NC–AF (0.01 mA cm^{-2}), highlighting the more favorable HER kinetics of Co–NC–AF enabled by the CoN_x active sites. To further assess the intrinsic activity of Co–NC–AF, its turnover frequency (TOF) was evaluated by assuming that each Co center account for one active site. The TOF value of Co–NC–AF at η = 100 mV was determined to be 0.153 s^{-1}, comparable to previously reported Co–N–C catalysts, such as Co–NG (0.101 s^{-1}),[38] for CoN_x–C (0.39 s^{-1}),[47] and Co–SAS/HOPNC (0.41 s^{-1}).[27] The areal number density of active sites in Co–NC–AF was estimated to be 3.53×10^{13} sites cm^{-2}.

The bubble releasing behaviors for Co–NC–AF, Co–NC–CF, and Pt foil at the current density of 100 mA cm^{-2} were recorded with a high-speed camera. For Co–NC–AF, massive amounts of generated H_2 bubbles rapidly escaped from the electrode and the majority (> 90%) of the detached bubbles were within the size of 0.2 mm (Figure 5d,e). In contrast, H_2 bubbles pinned strongly on the surface of Co–NC–CF and coalescence into large size (with more than half in the range of 0.3–0.5 mm) before leaving the surface. The Pt foil showed even stronger adhesion to H_2 bubbles, which were mainly (> 60%) distributed in the size range of >0.5 mm. The different bubble releasing behaviors of these electrodes can be ascribed to their distinct surface wettability.[42,48,49] With the superaerophobic feature, Co–NC–AF is able to release the H_2 bubbles in a timely manner and re-expose its catalytic sites to electrolyte (Movie S2, Supporting Information), making it feasible for continuous high-current H_2 generation.

The stability of Co–NC–AF was first evaluated by galvanostatic technique at constant current density of 200 mA cm^{-2}. The testing results show that Co–NC–AF can steadily and continuously deliver 200 mA cm^{-2} for at least 80 h and the overpotential increased slightly by ≈32 mV (from ≈210 to ≈242 mV) during the test (Figure S29, Supporting Information). In contrast, testing on Pt foil reveals that its activity dropped rapidly in the first 5 h due to the inefficiency to remove the accumulated bubbles (Figure S30, Supporting Information). XAFS studies on Co–NC–AF after stability test demonstrate that the cobalt elements remain in atomic dispersion without aggregation (Figure S31, Supporting Information), suggesting that the single-atom CoN_x sites are stable under the reductive potential of HER. SEM observation of the post-test electrode reveals that the porous frameworks and the vertical alignment of carbon structures were intact with no noticeable changes (Figure S32, Supporting Information), indicating that Co–NC–AF is mechanically robust to survive the interruption from the vigorous bubbling force. Further, the stability of Co–NC–AF was evaluated at higher current density of 1000 mA cm^{-2}. Impressively, Figure 5f shows that the overpotential remained almost the same with small fluctuation during the 32 h continuous electrolysis at 1000 mA cm^{-2}, and the polarization curve collected after the galvanostatic measurement almost overlapped with the initial one (Figure 5g), confirming the good durability of Co–NC–AF at high current density. It is noteworthy that the stability test was performed under static condition (i.e., without forced convection) to mimic the practical operation situation (see Movie S3, Supporting Information), which is enabled by the rapid removal of the vigorously evolved H_2 gases at the high current density of 1000 mA cm^{-2} from the surface of Co–NC–AF that would otherwise block the active sites and lead to degraded performance.

3. Conclusion

We have rationally designed an aligned porous film electrode decorated with single-atom Co–N–C sites for efficient electrocatalytic hydrogen production at high current densities. The atomic-scale CoN_x sites provide high intrinsic activity to enhance the HER kinetics. The aligned open microchannels and multiscale porosity facilitate the transport of ionic reactants and gaseous products under high mass loading and high reaction rate. The superhydrophilicity enables the film to be spontaneously wetted by electrolyte when immersed in aqueous solution, while the superaerophobicity renders the film with low adhesion to gas bubbles, favoring the rapid, and spontaneous removal of small-size H_2 bubbles. These designed features all together make the film capable of delivering industrial-level current density up to 1000 mA cm^{-2} with high activity and stability under realistic operating conditions, which is challenging to achieve in conventional powdery single-atom

M–N–C electrocatalysts. Considering the low metal loading of Co–NC–AF compared to previously reported nanoparticulate catalysts, future work would be directed to increase the contents of the CoN_x sites that can lead to further improvement of HER performance. Moreover, the synthetic methodology and design principle presented in this work could motivate the exploration of porous film-based M–N–C catalysts in wide ranges of technologically important gas-involving electrocatalytic processes (e.g., hydrogen oxidation reaction, oxygen evolution reaction, oxygen reduction reaction, CO_2 reduction reaction, N_2 reduction reaction) and put a step forward toward the practical applications of SACs.

4. Experimental Section

Materials: MWCNTs (>99.9 wt% purity; outer diameter 30–80 nm) were purchased from Chengdu Organic Chemicals Co. Ltd., while other chemicals were purchased from Sigma-Aldrich unless otherwise specified.

Preparation of O-MWCNTs: O-MWCNTs was synthesized by oxidizing MWCNTs under strongly acidic and oxidative conditions.[50] Briefly, MWCNTs (150 mg) were dispersed in 36 mL H_2SO_4 (98 wt%) and stirred for 1 h, followed by the addition of 4 mL H_3PO_4 (85 wt%) and stirring for another 15 min. Then, $KMnO_4$ (750 mg) was slowly added to the mixture and reacted at 65 °C for 2 h. After cooling to room temperature naturally, the mixture was poured into ice water (100 mL) containing 5 mL H_2O_2 (30 wt%) while stirring. The precipitate was washed several times with HCl (10 vol%), ethanol and water until the pH reached about 7.0. Finally, the precipitate was diluted with water to obtain aqueous solution of O-MWCNTs with desired concentrations.

Preparation of Co–NC–AF: First, a precursor solution was prepared consisting of O-MWCNTs and cobalt salt ($CoCl_2{\cdot}6H_2O$) (weight ratio of O-MWCNTs: Co = 135: 1) with mixture of H_2O (90 vol%) and ethanol (10 vol%) as the solvent. Afterward, the mixture was placed into a Teflon vessel for hydrothermal self-assembly at 120 °C for 12 h. The resulting hydrogel was sliced into thin films with different thicknesses and subjected to a directional-freezing process by putting on a copper plate that was precooled in liquid nitrogen. Finally, Co–NC–AF was obtained after being freeze-dried and annealed at 750 °C for 1 h in a tube furnace with the feeding of Ar (150 sccm) and NH_3 (50 sccm) at ambient pressure. It is noted that the weight ratio of O-MWCNTs: Co was varied to obtain the optimal catalytic activity of Co–NC–AF (Figure S33, Supporting Information).

Preparation of Co–NC–RF: Co–NC–RF was prepared with the same process as that of Co–NC–AF except for the freezing process that was performed in a refrigerator (–80 °C) to provide a uniform temperature gradient for nondirectional freezing.

Preparation of NC–AF: NC–AF was prepared with the same process as that of Co–NC–AF except that no cobalt salts were added in the precursor solution.

Preparation of Co–NC–CF: Co–NC–CF was prepared by first vacuum filtering 25 mL of precursor solution (2.0 mg mL^{-1} O-MWCNTs and 3.0 mg mL^{-1} $CoCl_2{\cdot}6H_2O$, weight ratio of O-MWCNTs:Co = 135:1) with a 0.45 mm hydrophilic polytetrafluoroethylene membrane. Then, the resulting film was dried at 70 °C for 10 h and annealed under the same conditions as Co–NC–AF.

Material Characterizations: The morphology and structure of the resulting materials were characterized by SEM (Hitachi S-4800 and COXEM EM-30 Plus), TEM (Titan G2 60-300), XRD (Bruker AXS, D8 Advance), and Raman spectra (InVia Reflex, Renishaw). Chemical compositions and elemental oxidation states of the samples were measured by XPS (Kratos Axis Supra) and the elemental spectra were all corrected with respect to C 1s peak at 284.8 eV. Quantitative analysis of metal loading was carried out using ICP-MS (Agilent 7900). The BET surface area and DFT pore size distribution were measured by Quantachrome NOVA 1000e. ADF STEM imaging and EDS characterizations were achieved using FEI Titan Cubed Themis G2 300 with a probe corrector. The CAs of water droplets on the sample surfaces were recorded by a contact angle measuring device (LSA100, LAUDA Scientific, Germany). The volume of the water droplet was 3 µL for each test. The CAs of gas bubbles under water were tested by the captive-bubble method (LSA100, LAUDA Scientific, Germany).[42] The volume of the gas bubble was 5 µL for each test. Adhesive force between the gas bubble and the electrode surfaces was measured by a high-sensitivity microelectromechanical balance system (Lauda Scientific LSA100, Germany).[43]

XAFS Characterization: X-ray absorption spectra at Co K-edge were acquired under ambient condition in fluorescence mode using a Si (111) double-crystal monochromator at 1W1B beamline of Beijing Synchrotron Radiation Facility and 14W1 beamline of the Shanghai Synchrotron Radiation Facility. The incident and fluorescence X-ray intensities were monitored by using standard N_2-filled ion chambers and Ar-filled Lytle-type detector, respectively. The XAFS raw data were background-subtracted, normalized, and Fourier transformed by the standard procedures with the ATHENA program, and least-squares curve fitting analysis of the EXAFS $\chi(k)$ data was carried out using the ARTEMIS program based on the standard EXAFS equation.[51] All fits were performed in the R space with k-weight of 2.

Electrochemical Measurements: The electrochemical measurements were performed in 0.5 M H_2SO_4 by a CHI 760E electrochemical workstation (Shanghai Chenhua Instrument Co.) with $Hg/HgSO_4$ reference electrode (Wuhan Gaoss Union Co. Ltd.) and graphite rod counter electrode (60 mm in length, 6 mm in diameter, Wuhan Gaoss Union Co. Ltd.). Before each test, the electrolyte was purged with N_2 for at least 20 min to remove the dissolved O_2. The measured potential against reference electrode was converted to reversible hydrogen electrode (RHE) by $E_{RHE} = E_{Hg/HgSO4} + 0.674$ based on the calibration results. For the film-based electrodes (Co–NC–AF, Co–NC–RF, Co–NC–CF, and NC–AF), they were directly used as working electrodes and back-contacted with a glassy carbon substrate (diameter = 8 mm) using carbon adhesives. The carbon adhesives were home-made by mixing MWCNTs (> 99.9 wt% purity; outer diameter 30–80 nm) and 5 wt% Nafion solution in a 9:1 weight ratio. The optimized electrode of Co–NC–AF has a thickness of 1.5 mm and areal mass loading of 6.0 mg cm^{-2}. The electrode of Co–NC–Slurry was prepared by the following steps: 10 mg Co–NC–AF catalyst, 1 mL ethanol and 100 µL 5 wt% Nafion solution were mixed with sonication to form a catalyst ink, which was then drop-cast on a carbon fiber paper (Toray TGP-H-060) to give a loading density of 3.5 mg cm^{-2}. Further increasing the loading would lead to cracking of the catalyst film after drying. Commercial Pt/C (20 wt%, Johnson Matthey) on glassy carbon electrode (diameter = 5 mm) was prepared by a drop-casting method with an optimized mass loading of 1 mg cm^{-2} (Figure S34, Supporting Information). The LSV polarization curves were recorded at a scan rate of 5 mV s^{-1}. All polarization curves were corrected for background current and iR losses (100% compensation level), as detailed in Figure S35 (Supporting Information), unless otherwise specified. The corresponding Tafel plots were obtained by fitting the linear portion between the overpotential (η) and log current density (log-j), using the equation $\eta = b \log(j) + a$, where b is the Tafel slope. The electrochemical double layer capacitance (C_{dl}) was derived from CV curves at non-Faradaic region (from 0.05 to 0.25 V vs RHE) at various scan rates of 20, 40, 60, 80, and 100 mV s^{-1}. The obtained current densities at the selected potential have the linear relationship with the scan rates and the slopes of fitting curves were considered as the C_{dl}, see Figure S12 (Supporting Information) and Figure 2j. EIS was measured by AC impedance spectroscopy in potentiostatic mode at the overpotential of 30 mV, applying a sinusoidal voltage with an amplitude of 10 mV and scanning frequency from 100 kHz to 0.1 Hz. Faradaic efficiency is defined as the ratio of H_2 amount collected by water drainage method to the amount in theory (Figure S22, Supporting Information). The stability was evaluated by galvanostatic technique in 0.5 M H_2SO_4 solution at constant current density of 200 or 1000 mA cm^{-2} without stirring or N_2-purging to mimic the practical operation.

Supporting Information

Supporting Information is available from the Wiley Online Library or from the author.

Acknowledgements

R.L. and Z.G. contributed equally to this work. H.F. acknowledges financial support from the National Natural Science Foundation of China (Grant No. 51902099), Hunan high-level talent gathering project (Grant No. 2019RS1021), Fundamental Research Funds for the Central Universities (Grant No. 531119200087), and the Innovative Research Groups of Hunan Province (Grant No. 2020JJ1001). G.Y. acknowledges support from the Hunan Province Natural Science Foundation (Grant No. 2020JJ4204). J.D. acknowledges support from Youth Innovation Promotion Association CAS.

Conflict of Interest

The authors declare no conflict of interest.

Data Availability Statement

The data that support the findings of this study are available from the corresponding author upon reasonable request.

Keywords

electrocatalysis, graphene, high current density, hydrogen evolution reaction, porous films, single-atom catalysts

Received: May 10, 2021
Revised: July 8, 2021
Published online:

[1] D. H. Kweon, M. S. Okyay, S.-J. Kim, J.-P. Jeon, H.-J. Noh, N. Park, J. Mahmood, J.-B. Baek, *Nat. Commun.* **2020**, *11*, 1278.
[2] M. F. Lagadec, A. Grimaud, *Nat. Mater.* **2020**, *19*, 1140.
[3] Q. Cheng, C. Hu, G. Wang, Z. Zou, H. Yang, L. Dai, *J. Am. Chem. Soc.* **2020**, *142*, 5594.
[4] J. Zhu, L. Hu, P. Zhao, L. Y. S. Lee, K.-Y. Wong, *Chem. Rev.* **2020**, *120*, 851.
[5] Y. Zhao, C. Chang, F. Teng, Y. Zhao, G. Chen, R. Shi, G. I. N. Waterhouse, W. Huang, T. Zhang, *Adv. Energy Mater.* **2017**, *7*, 1700005.
[6] J. Wang, Y. Gao, H. Kong, J. Kim, S. Choi, F. Ciucci, Y. Hao, S. Yang, Z. Shao, J. Lim, *Chem. Soc. Rev.* **2020**, *49*, 9154.
[7] H. Zhou, F. Yu, Q. Zhu, J. Sun, F. Qin, L. Yu, J. Bao, Y. Yu, S. Chen, Z. Ren, *Energy Environ. Sci.* **2018**, *11*, 2858.
[8] W. Ju, M. V. F. Heinz, L. Pusterla, M. Hofer, B. Fumey, R. Castiglioni, M. Pagani, C. Battaglia, U. F. Vogt, *ACS Sustainable Chem. Eng.* **2018**, *6*, 4829.
[9] S. Xue, Z. Liu, C. Ma, H.-M. Cheng, W. Ren, *Sci. Bull.* **2020**, *65*, 123.
[10] C. Zhang, Y. Luo, J. Tan, Q. Yu, F. Yang, Z. Zhang, L. Yang, H.-M. Cheng, B. Liu, *Nat. Commun.* **2020**, *11*, 3724.
[11] Y. Wang, J. Mao, X. Meng, L. Yu, D. Deng, X. Bao, *Chem. Rev.* **2019**, *119*, 1806.
[12] S. K. Kaiser, Z. Chen, D. Faust Akl, S. Mitchell, J. Pérez-Ramírez, *Chem. Rev.* **2020**, *120*, 11703.
[13] A. Wang, J. Li, T. Zhang, *Nat. Rev. Chem.* **2018**, *2*, 65.
[14] J. Wang, Z. Li, Y. Wu, Y. Li, *Adv. Mater.* **2019**, *30*, 1801649.
[15] Y. Peng, B. Lu, S. Chen, *Adv. Mater.* **2018**, *30*, 1801995.
[16] Y. Yang, Y. Yang, Z. Pei, K.-H. Wu, C. Tan, H. Wang, L. Wei, A. Mahmood, C. Yan, J. Dong, S. Zhao, Y. Chen, *Matter* **2020**, *3*, 1442.
[17] J. Li, M. T. Sougrati, A. Zitolo, J. M. Ablett, I. C. Oğuz, T. Mineva, I. Matanovic, P. Atanassov, Y. Huang, I. Zenyuk, A. Di Cicco, K. Kumar, L. Dubau, F. Maillard, G. Dražić, F. Jaouen, *Nat. Catal.* **2021**, *4*, 10.
[18] M. Primbs, Y. Sun, A. Roy, D. Malko, A. Mehmood, M.-T. Sougrati, P.-Y. Blanchard, G. Granozzi, T. Kosmala, G. Daniel, P. Atanassov, J. Sharman, C. Durante, A. Kucernak, D. J. Jones, F. Jaouen, P. Strasser, *Energy Environ. Sci.* **2020**, *13*, 2480.
[19] L. Cao, Q. Luo, W. Liu, Y. Lin, X. Liu, Y. Cao, W. Zhang, Y. Wu, J. Yang, T. Yao, S. Wei, *Nat. Catal.* **2019**, *2*, 134.
[20] S. Ji, Y. Chen, X. Wang, Z. Zhang, D. Wang, Y. Li, *Chem. Rev.* **2020**, *120*, 11900.
[21] Y. Lei, Y. Wang, Y. Liu, C. Song, Q. Li, D. Wang, Y. Li, *Angew. Chem., Int. Ed.* **2020**, *59*, 20794.
[22] S. Ye, F. Luo, Q. Zhang, P. Zhang, T. Xu, Q. Wang, D. He, L. Guo, Y. Zhang, C. He, X. Ouyang, M. Gu, J. Liu, X. Sun, *Energy Environ. Sci.* **2019**, *12*, 1000.
[23] Z. Pu, I. S. Amiinu, R. Cheng, P. Wang, C. Zhang, S. Mu, W. Zhao, F. Su, G. Zhang, S. Liao, S. Sun, *Nano-Micro Lett.* **2020**, *12*, 21.
[24] Y. Wang, H. Su, Y. He, L. Li, S. Zhu, H. Shen, P. Xie, X. Fu, G. Zhou, C. Feng, D. Zhao, F. Xiao, X. Zhu, Y. Zeng, M. Shao, S. Chen, G. Wu, J. Zeng, C. Wang, *Chem. Rev.* **2020**, *120*, 12217.
[25] H. Fei, J. Dong, D. Chen, T. Hu, X. Duan, I. Shakir, Y. Huang, X. Duan, *Chem. Soc. Rev.* **2019**, *48*, 5207.
[26] D. Malko, A. Kucernak, T. Lopes, *Nat. Commun.* **2016**, *7*, 13285.
[27] T. Sun, S. Zhao, W. Chen, D. Zhai, J. Dong, Y. Wang, S. Zhang, A. Han, L. Gu, R. Yu, X. Wen, H. Ren, L. Xu, C. Chen, Q. Peng, D. Wang, Y. Li, *Proc. Natl. Acad. Sci. USA* **2018**, *115*, 12692.
[28] X. Wan, X. Liu, Y. Li, R. Yu, L. Zheng, W. Yan, H. Wang, M. Xu, J. Shui, *Nat. Catal.* **2019**, *2*, 259.
[29] Y. Kuang, C. Chen, D. Kirsch, L. Hu, *Adv. Energy Mater.* **2019**, *9*, 1901457.
[30] Y. He, S. Liu, C. Priest, Q. Shi, G. Wu, *Chem. Soc. Rev.* **2020**, *49*, 3484.
[31] J. Yang, A. R. Mohmad, Y. Wang, R. Fullon, X. Song, F. Zhao, I. Bozkurt, M. Augustin, E. J. G. Santos, H. S. Shin, W. Zhang, D. Voiry, H. Y. Jeong, M. Chhowalla, *Nat. Mater.* **2019**, *18*, 1309.
[32] X. Zhao, H. Ren, L. Luo, *Langmuir* **2019**, *35*, 5392.
[33] Q. Song, Z. Xue, C. Liu, X. Qiao, L. Liu, C. Huang, K. Liu, X. Li, Z. Lu, T. Wang, *J. Am. Chem. Soc.* **2020**, *142*, 1857.
[34] W. Xu, Z. Lu, X. Sun, L. Jiang, X. Duan, *Acc. Chem. Res.* **2018**, *51*, 1590.
[35] X. Shan, J. Liu, H. Mu, Y. Xiao, B. Mei, W. Liu, G. Lin, Z. Jiang, L. Wen, L. Jiang, *Angew. Chem., Int. Ed.* **2020**, *59*, 1659.
[36] Y. Li, T. Gao, Y. Yao, Z. Liu, Y. Kuang, C. Chen, J. Song, S. Xu, E. M. Hitz, B. Liu, R. J. Jacob, M. R. Zachariah, G. Wang, L. Hu, *Adv. Energy Mater.* **2018**, *8*, 1801289.
[37] I. V. Thorat, D. E. Stephenson, N. A. Zacharias, K. Zaghib, J. N. Harb, D. R. Wheeler, *J. Power Sources* **2009**, *188*, 592.
[38] H. Fei, J. Dong, M. J. Arellano-Jiménez, G. Ye, N. D. Kim, E. L. G. Samuel, Z. Peng, Z. Zhu, F. Qin, J. Bao, M. J. Yacaman, P. M. Ajayan, D. Chen, J. M. Tour, *Nat. Commun.* **2015**, *6*, 8668.
[39] H. Fei, J. Dong, Y. Feng, C. S. Allen, C. Wan, B. Volosskiy, M. Li, Z. Zhao, Y. Wang, H. Sun, P. An, W. Chen, Z. Guo, C. Lee, D. Chen, I. Shakir, M. Liu, T. Hu, Y. Li, A. I. Kirkland, X. Duan, Y. Huang, *Nat. Catal.* **2018**, *1*, 63.

[40] H. Fei, J. Dong, C. Wan, Z. Zhao, X. Xu, Z. Lin, Y. Wang, H. Liu, K. Zang, J. Luo, S. Zhao, W. Hu, W. Yan, I. Shakir, Y. Huang, X. Duan, *Adv. Mater.* **2018**, *30*, 1802146.
[41] Y. Luo, L. Tang, U. Khan, Q. Yu, H.-M. Cheng, X. Zou, B. Liu, *Nat. Commun.* **2019**, *10*, 269.
[42] Z. Lu, W. Zhu, X. Yu, H. Zhang, Y. Li, X. Sun, X. Wang, H. Wang, J. Wang, J. Luo, X. Lei, L. Jiang, *Adv. Mater.* **2014**, *26*, 2683.
[43] Y. Li, H. Zhang, T. Xu, Z. Lu, X. Wu, P. Wan, X. Sun, L. Jiang, *Adv. Funct. Mater.* **2015**, *25*, 1737.
[44] T. Y. Ma, S. Dai, S. Z. Qiao, *Mater. Today* **2016**, *19*, 265.
[45] L. Tang, R. Xu, J. Tan, Y. Luo, J. Zou, Z. Zhang, R. Zhang, Y. Zhao, J. Lin, X. Zou, B. Liu, H.-M. Cheng, *Adv. Funct. Mater.* **2020**, *31*, 2006941.
[46] Y. Chen, G. Yu, W. Chen, Y. Liu, G.-D. Li, P. Zhu, Q. Tao, Q. Li, J. Liu, X. Shen, H. Li, X. Huang, D. Wang, T. Asefa, X. Zou, *J. Am. Chem. Soc.* **2017**, *139*, 12370.
[47] H.-W. Liang, S. Brüller, R. Dong, J. Zhang, X. Feng, K. Müllen, *Nat. Commun.* **2015**, *6*, 7992.
[48] H. Li, S. Chen, Y. Zhang, Q. Zhang, X. Jia, Q. Zhang, L. Gu, X. Sun, L. Song, X. Wang, *Nat. Commun.* **2018**, *9*, 2452.
[49] X. Yu, Z.-Y. Yu, X.-L. Zhang, Y.-R. Zheng, Y. Duan, Q. Gao, R. Wu, B. Sun, M.-R. Gao, G. Wang, S.-H. Yu, *J. Am. Chem. Soc.* **2019**, *141*, 7537.
[50] A. L. Higginbotham, D. V. Kosynkin, A. Sinitskii, Z. Sun, J. M. Tour, *ACS Nano* **2010**, *4*, 2059.
[51] B. Ravel, M. Newville, *J. Synchrotron Radiat.* **2005**, *12*, 537.